Earth and Planetary Science Letters 532 (2020) 116040

Contents lists available at ScienceDirect

Earth and Planetary Science Letters

www.elsevier.com/locate/epsl

Upper mantle and mantle transition zone thermal and water content anomalies beneath NE Asia: Constraints from receiver function imaging of the 410 and 660 km discontinuities

Muchen Sun[a,b,c], Stephen S. Gao[c,*], Kelly H. Liu[c], Xiaofei Fu[a]

[a] College of Earth Science and Research Institute of Unconventional Oil and Gas, Northeast Petroleum University, Daqing, Heilongjiang 163318, China
[b] State Key Laboratory of Marine Geology, Tongji University, Shanghai 200092, China
[c] Geology and Geophysics Program, Missouri University of Science and Technology, Rolla, MO 65409, USA

ARTICLE INFO

Article history:
Received 27 June 2019
Received in revised form 10 December 2019
Accepted 14 December 2019
Available online 6 January 2020
Editor: M. Ishii

Keywords:
mantle transition zone
receiver function
subduction
mantle plume
Northeast Asia
Cenozoic volcanism

ABSTRACT

The 410 and 660 km discontinuities (*d*410 and *d*660) bordering the mantle transition zone (MTZ) beneath NE Asia, including NE China, Eastern Mongolia, and southern Siberia, are imaged in successive circular bins with a radius of 1 degree by stacking a total of 274,413 *P*-to-*s* radial receiver functions recorded by 799 broadband seismic stations. After moveout correction based on the 1-D IASP91 Earth model, the resulting apparent depths of the discontinuities exhibit significant and spatially systematic variations. Three approximately N-S elongated narrow zones with significantly thickened MTZ are observed, which may be associated with the thermal effect and dehydration of subducted slabs. The major volcanoes in NE China are underlain by a *d*660 that is apparently depressed by ~19 km, which can be interpreted by the presence of an anomalously high water concentration in the lower MTZ released from the stagnated slabs. Low wavespeed anomalies above the *d*410 west of the Datong volcanic fields are underlain by an MTZ with normal thickness, and are attributable by dehydration of the leading portion of the stagnant Pacific slab in the MTZ that is revealed in an N-S oriented narrow zone east of this area. The lateral shift of the upper mantle low wavespeed zone and the area with thickened MTZ may suggest a westward drift of the upper mantle relative to the subducted slab. An abnormally thin MTZ is observed beneath the Hangay Dome in central Mongolia, suggesting the possible existence of thermal upwelling from the lower mantle through the MTZ.

1. Introduction

Subduction of the Pacific Plate beneath the eastern margin of the Eurasian Plate started during late Jurassic and Cretaceous (Sun et al., 2007). Under the assumption that the subduction rate over the past ~130 million years is similar to the current rate of 90 mm/yr (Gripp and Gordon, 2002), a total of ~12,000 km of Pacific lithosphere has subducted. In NE Asia, the subducted Pacific slab has been identified by many seismic tomographic studies (e.g., Chen et al., 2017; Tang et al., 2014) as a high wavespeed zone of about 150 km thick in the upper mantle. In the mantle transition zone (MTZ), which is the layer between the 410 km (*d*410) and 660 km (*d*660) discontinuities, most seismic tomography studies (Huang and Zhao, 2006; Lei, 2012) image the stagnant slab as a sub-horizontal layer of high wavespeeds with a thickness of about 100–200 km, and suggest that the westernmost fragment of the horizontally deflected slab in the MTZ has reached the Great Xing'an Range (Fig. 1).

Intraplate Cenozoic volcanoes in NE China are mainly distributed along the edges of the Songliao basin (Fig. 1). In spite of numerous studies aiming at understanding the origins of these volcanoes (Tang et al., 2014; Turcotte and Schubert, 1982; Wei et al., 2019), the physical and chemical processes responsible for their formation remain enigmatic. Turcotte and Schubert (1982) suggest that the Changbaishan volcanoes might be associated with a mantle plume, while some recent tomographic studies (e.g., Wei et al., 2019) attribute them to wet and hot upwelling from dehydration of the subducted Pacific slab.

Some other studies (e.g., Tang et al., 2014; Liu et al., 2015) interpret the Changbaishan volcanoes as the consequence of subduction-induced upwelling through a slab gap. Besides the Changbaishan, the origin of other Cenozoic volcanoes in NE China including the Wudalianchi and Halaha is also debated. Geochem-

---

[*] Corresponding author.
E-mail address: sgao@mst.edu (S.S. Gao).

https://doi.org/10.1016/j.epsl.2019.116040

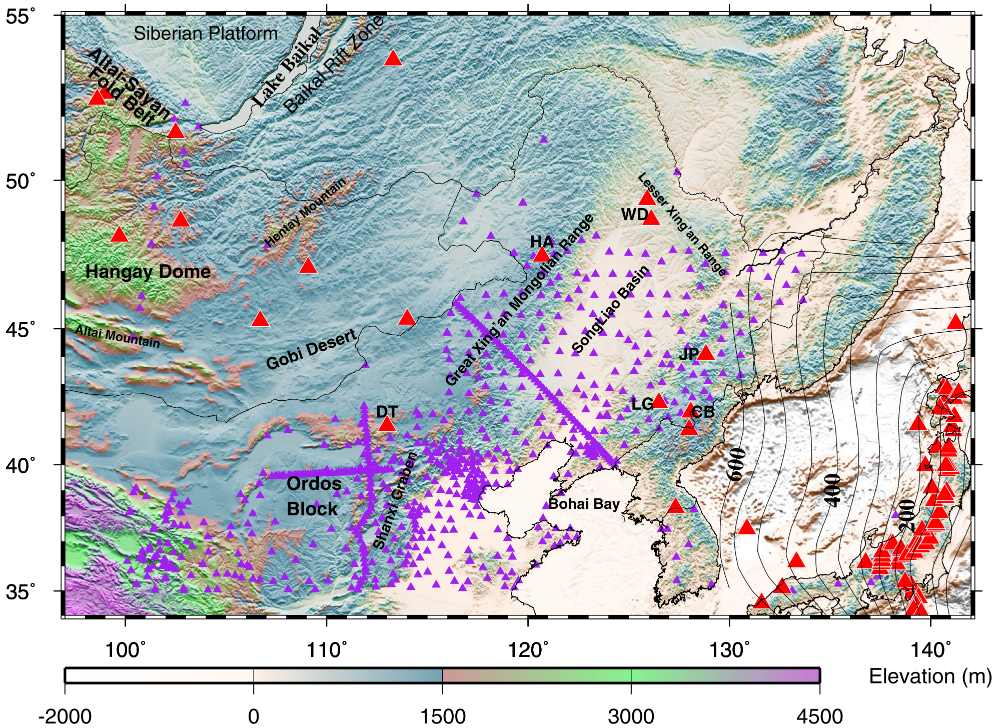

Fig. 1. Topographic relief map of NE Asia showing the distribution of seismic stations used in the study (purple triangles), major tectonic provinces, depth contours of the subducting Pacific slab (Gudmundsson and Sambridge, 1998) and Cenozoic volcanoes (red triangles). CB-Changbaishan, LG-LongGang, JP-Jingpohu, WD-Wudalianchi, HA-Halaha, DT-Datong. (For interpretation of the colors in the figure(s), the reader is referred to the web version of this article.)

ical investigations (Kuritani et al., 2013) suggest that the Wudalianchi volcano is associated with a hydrous mantle plume originating from the hydrated MTZ, while others (e.g., Zhang et al., 1998) attribute it to shallower processes. A recent seismic tomography study (Wei et al., 2019) reveals high wavespeed anomalies in the MTZ beneath the Wudalianchi and Halaha volcanoes, and that most other areas in NE China are underlain by low wavespeeds in the upper mantle. Wei et al. (2019) propose that the Wudalianchi volcano is fed by a wet upwelling from the stagnant Pacific slab in the MTZ, while the Halaha volcano, which is located above the leading edge of the Pacific slab, is associated with a focused upwelling caused by the sinking of the stagnant Pacific slab into the lower mantle.

Similarly, in spite of numerous studies (Huang and Zhao, 2006; Kuritani et al., 2013; Lei, 2012; Li et al., 2018), the formation mechanism of the Datong volcanoes, which are located at the northeastern edge of the Ordos block, remains controversial. Huang and Zhao (2006) find low wavespeed anomalies beneath the Datong volcanoes, and suggest that they were probably caused by dehydration of the stagnant Pacific slab in the MTZ. Lei (2012) attributes the Datong volcanoes to a lower mantle plume that travels through the slab gap to the uppermost mantle. Li et al. (2018) suggest that the Datong volcanoes are fed by decompression partial melting associated with the asthenosphere flowing upward following the eastward thinning lithosphere.

Beside the Cenozoic volcanoes, another significant tectonic feature in NE Asia is the Baikal rift zone (BRZ) located between the Siberian platform and the Altai-Sayan fold belt (Fig. 1) and is seismically the most active continental rift on Earth. The BRZ is characterized by high heat flow (Lysak, 1984), lower than normal mantle wavespeeds (Gao et al., 2003), significant crustal thinning (Gao et al., 2004), and negative gravity anomalies (Zorin et al., 2003). Although most tomographic studies (e.g., Gao et al., 2003) found low wavespeed anomalies beneath the BRZ and adjacent areas, the depth extent of this anomaly remains highly divergent in different studies. Some studies support an active rifting model, which is characterized by an active thermal upwelling (e.g., Zorin et al., 2003), while others favor a passive origin that is induced by the driving forces from the collision between the Indian and Eurasian plates (e.g., Yin, 2000).

Another controversial issue in the study area is the cause of the anomalously high topography of the Hangay Dome in central Mongolia (Fig. 1). Some studies suggest that the high elevation of the Hangay Dome is the result of thermal upwelling from the lower mantle impinged on the bottom of the lithosphere (Chen et al., 2015; Zhang et al., 2017; Zorin et al., 2003), probably associated with a mantle plume, and other studies (e.g., Mordvinova et al., 2015) propose that lithospheric delamination induced convective asthenospheric upwelling is responsible for the anomalously elevated topography.

Most of the aforementioned controversies stem from the limited vertical resolution of the tomographic inversion techniques especially in the MTZ depth (Foulger et al., 2013), as well as the progressive temperature increase of the subducted slabs which gradually reduces the wavespeed contrast between the slabs and ambient mantle, making it difficult for seismic tomography studies to reliably image the slabs. The opposite effects of hydration and low temperature that may co-exist in subducted slabs on seismic wavespeeds may also play a role in the ambiguities in the interpretation of the seismic images (Garth and Rietbrock, 2017). Numerous mineral physical, geodynamic modeling, and geophysical observational investigations have demonstrated that in-situ temperature and presence of water in the MTZ can be revealed by the topography of the $d410$ and $d660$, which represent the phase transition from olivine to spinel, and from ringwoodite to Mg-perovskite + magnesiowustite, respectively (Ringwood, 1975). The former transition has a positive Clapeyron slope, suggesting that a region of cold temperature results in an uplift of the $d410$ and vice versa, while the latter has a negative Clapeyron slope. The actual magnitude of the Clapeyron slopes, especially that associated with the $d660$, is debated (Bina and Helffrich, 1994; Fei et al., 2004; Ghosh et al., 2013). Recent studies suggest that water has a similar effect on the topography of the MTZ discontinuities as low temperature, but the existence of water in the lower MTZ has a much more significant impact on the depression of the *d*660 than low temperature (Ghosh et al., 2013). Consequently, significant depressions of the *d*660 are indicative of the existence of a hydrous lower MTZ (Ghosh et al., 2013).

A number of MTZ studies have been conducted in various regions of NE Asia to investigate the thermal state and the presence of water in the MTZ. Ai et al. (2003) and Li and Yuan (2003) image the MTZ structure beneath NE China using broadband stations. Both studies show a regionally depressed *d*660 and thickened MTZ, suggesting that the Pacific slab exists in the MTZ and has reached the lower mantle. Another MTZ study (Liu et al., 2015) measures the depth variation of the MTZ discontinuities beneath NE China based on different wavespeed models, and finds a NNW-SSE elongated region with thickened MTZ due to the significant depression of the *d*660 (∼40 km) in the southern part of NE China and a thinner than normal MTZ at about 200 km west to the Changbaishan volcanoes, indicating the absence of cold slabs in the MTZ and that the volcanoes might be fed by thermal upwelling from the lower mantle rather than slab dehydration. In contrast, Tian et al. (2016) reveal a thicker than normal MTZ beneath the Changbaishan volcanoes and attribute their formation to dehydration of the subducting Pacific slab in the MTZ. The MTZ study in NE China conducted by Zhang et al. (2016), which utilized over 90,000 receiver functions recorded by 584 broadband seismic stations, reveals successfully that the Pacific slab penetrated into the lower mantle after accumulation above the *d*660 beneath NE China, and the absence of the stagnant slab in the MTZ beneath North China Craton. However, Chen and Ai (2009) found an up to 20–30 km thicker-than-normal MTZ on the eastern side of the north-south gravity lineament beneath the North China Craton, which is interpreted by the influence of the deep subduction and stagnation of the Pacific slab. Beneath the BRZ, Liu and Gao (2006) reveal an uplifted *d*410 which favors a passive rifting mechanism. Si et al. (2013) utilize receiver functions from two stations in the vicinity of the BRZ to image the MTZ discontinuities beneath the BRZ, and find depressed MTZ discontinuities and an about 40 km thickening beneath the BRZ except for a small area with an MTZ thinning up to 20 km in magnitude. They indicate that the development of the BRZ is dominated by the detachment of the lithosphere and the consequent hot upwelling. Using seismic data from three stations, Chen et al. (2015) report an MTZ that is 10–20 km thinner than the globally averaged value of 250 km beneath the Hangay Dome, and interpret it as the consequence of a slightly warmer thermal anomaly across the MTZ.

Following a receiver function (RF) stacking procedure (Gao and Liu, 2014a) developed under the assumption of non-plane wavefront, which is capable of more accurately imaging the *d*410 and *d*660 than procedures assuming a plane wavefront, this study utilizes an unprecedentedly large number (274,413) of *P*-to-*s* receiver functions to produce robust images of the MTZ discontinuities beneath NE Asia, for the purpose of providing additional constraints on a number of tectonically significant and controversial issues related to slab subduction and thermal upwelling.

2. Data and methods

2.1. Data

The broadband teleseismic data employed in the study were recorded by 799 stations in the study area (97°E to 142°E, and 37°N to 54°N) belonging to a total of 35 different seismic networks (Fig. 1). The recording duration for the stations is from mid-1986 to September-2018. To achieve an optimal balance between the quality and quantity of the requested data, a variable cut-off magnitude (M_c) is calculated based on the empirical equation, $M_c = 5.2 + (\Delta - 30.0)/(180.0 - 30.0) - D/700.0$, where Δ and D represent the epicentral distance (ranging from 30° to 100°) in degree and focal depth in kilometer, respectively.

2.2. Data processing

A detailed description of the procedure for data selection, preprocessing, moveout correction, and stacking under a non-plane-wave assumption can be found in the MTZ discontinuity study of the contiguous United States (Gao and Liu, 2014b), and is briefly described below. A band-pass filter with corner frequencies 0.02 and 0.2 Hz was applied to filter the requested seismograms, and those with a first-arrival signal-to-noise ratio (SNR) of 4.0 or greater on the vertical-component seismograms were converted into radial receiver functions (RFs) following the procedure of Ammon (1991). To test the robustness of the results, a different band-pass filter with corner frequencies 0.03 and 0.3 Hz that was used by Ai et al. (2003) was also applied. Then visually checking was performed for all the resulting RFs to reject the ones with abnormal arrivals or no clear first *P* pulse. Finally, a total of 274,413 RFs from 10,118 events were used (Fig. S1), a quantity that is unmatched by any *P*-to-*s* RF studies in the area.

To stack the RFs (Dueker and Sheehan, 1997), the coordinates of the ray-piercing points of the *P*-to-*s* converted phase at the depth of 535 km (which is approximately the center of the MTZ) were first calculated (Fig. S2), and the RFs with piercing points in each of the radius=1° circular bins were moveout corrected and stacked to form a depth series using the IASP91 Earth model (Kennett and Engdahl, 1991). Note that we also grouped the RFs separately at the 410 and 660 km depths, and the resulting discontinuity depths are within 2 km for the vast majority of the bins. The distance between neighboring bins is 1 geographic degree, and therefore, there is an overlap among neighboring bins. To ensure reliability, results from bins with less than 10 RFs were not used. For each bin, a bootstrap resampling procedure with 50 resampling iterations (Efron and Tibshirani, 1986) was employed to calculate the mean and standard deviation of the MTZ discontinuity depths and MTZ thickness.

Since the RFs were moveout-corrected utilizing the 1-D IASP91 Earth model, the resulting MTZ discontinuity depths are apparent rather than true depths. In this study, following the wavespeed correction procedure of Gao and Liu (2014b), we used a regional (Chen et al., 2017) and one global wavespeed model (Lu et al., 2019) to correct the apparent depths.

3. Results

A total of 655 bins render robust determinations of at least one of the two MTZ discontinuities (Fig. 2), including 652 bins for the *d*410, 645 bins for the *d*660, and 642 bins for both (Table S1). As a result of the high quality and quantity of the RFs, the *d*410 and *d*660 arrivals are unambiguously identified for virtually all the bins, except for a few of them on the edges of the study area. Fig. 3 shows an E-W profile centered at the 43°N latitude, and all the depth series along the 21 E-W profiles can be found in Fig. S3. An E-W profile centered at the 43°N latitude using RFs filtered in the frequency band of 0.03–0.3 Hz can be found in Fig. S4, which shows similar characteristics of the discontinuities to those shown in Fig. 3.

The resulting *d*410 apparent depths range from 377 to 444 km with a mean value of 415.9 ± 8.2 km, and for the *d*660, the corresponding values are 637 to 709 km and 669.5 ± 10.0 km, respectively. The observed MTZ thickness ranges from 211 to 296 km, with a mean value of 253.2 ± 9.4 km, which is ∼3 km thicker than

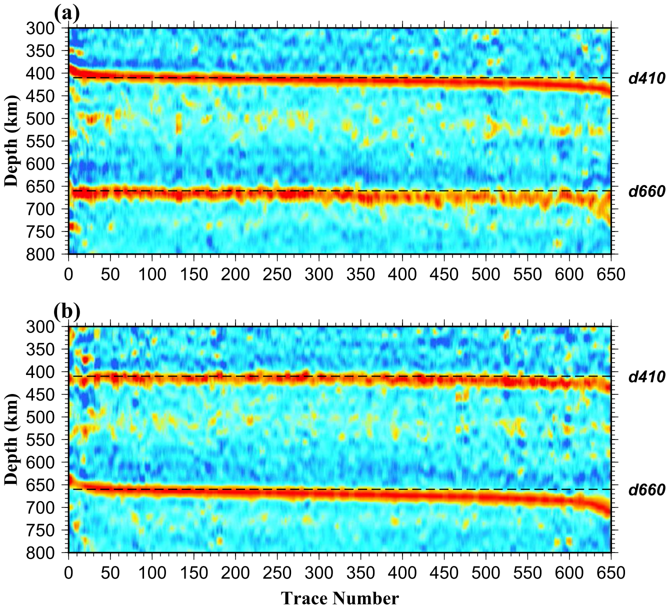

Fig. 2. (a) Depth series in 1° radius bins plotted with respect to the sequentially increasing depth of the $d410$. (b) Same as (a) but for sequentially increasing depth of the $d660$.

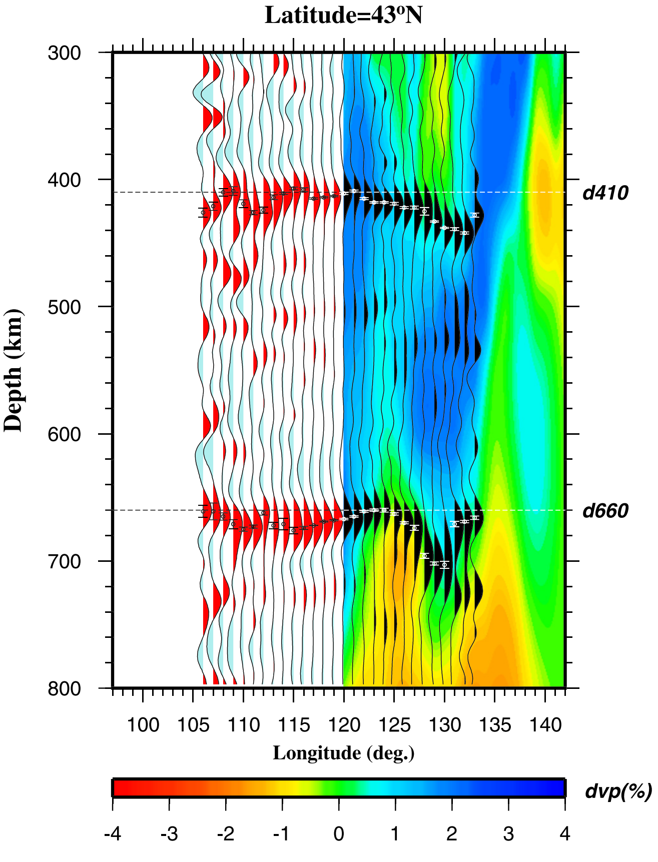

Fig. 3. Stacked receiver functions across the 43°N latitudinal line and $d410$ and $d660$ arrivals (dots with error bars). The background image shows P-wavespeed anomalies (Chen et al., 2017), which only reliably cover the area east of 120°E. The vertical exaggeration factor is about 10.

the global average of 250 km in the IASP91 Earth model. A continuous curvature surface gridding algorithm with a tension factor of 0.5 was used to obtain the spatially continuous images of the discontinuity depths and MTZ thickness (Fig. 4).

Accurate true MTZ discontinuity depths can only be obtained when absolute (rather than relative to the mean values of a study area) wavespeed anomalies of both the P and S waves are available for the entire crust, upper mantle, and MTZ. The cross-correlation coefficient (XCC) between MTZ discontinuities, which reflects the similarity of the depth variation between $d410$ and $d660$, can be an effective indicator of the accuracy of the wavespeed correction (Gao and Liu, 2014b). The XCC is defined as $Cov(d410, d660)/\sqrt{v(d410) \times v(d660)}$. Here, the $Cov(d410, d660)$ is the covariance of the depths of the two MTZ discontinuities, and $v(d410)$ and $v(d660)$ are the variances of the depths of the $d410$ and $d660$, respectively. The wavespeed anomalies above the $d410$ can lead to positive correlations between the apparent depths of $d410$ and $d660$, while thermal and water content anomalies in the MTZ theoretically result in negative correlations between the corrected depths of the two MTZ discontinuities. Therefore, if there are no thermal, water content, or other anomalies affecting the true depths of the MTZ discontinuities, the resulting XCC between the corrected depths should reduce to zero. In contrast, if thermal or water content anomalies exist in the MTZ, the XCC should be a negative value. The XCC between the apparent MTZ discontinuity depths in the study area is 0.48 (Fig. 5), which is significant lower than 0.84 for the contiguous United States (Gao and Liu, 2014b) and 0.7 for southern Africa (Sun et al., 2018), indicating the presence of significant thermal, water content or wavespeed anomalies in the MTZ. One global and one regional wavespeed models (Lu et al., 2019; Chen et al., 2017) are employed for wavespeed correction in this study. The averaged P-wavespeed anomalies above the $d410$ and in the MTZ from these two tomographic models are shown in Fig. 6, and the corrected $d410$ and $d660$ depths and MTZ thickness are shown in Fig. 7. The considerable differences in the corrected depths are indicative of the significant discrepancies of the wavespeed models. The low effectiveness of the wavespeed correction is also reflected in the limited reduction in the XCC between the corrected $d410$ and $d660$ depths from the original value of 0.48 to 0.42 for the wavespeed model of Lu et al. (2019), and no significant reduction of XCC between the corrected $d410$ and $d660$ depths for the regional wavespeed model (Chen et al., 2017). In the following we discuss the thermal, water, and wavespeed structure based on both the apparent and corrected depths. According to the patterns of the resulting discontinuity depths and MTZ thickness, we selected seven subareas with significantly different measurements from the global averages for discussion (Fig. 4), and the averaged measurements for each of the subareas are shown in Table S2. It is worth mentioning that because the regional tomographic results east of 120°E and south of 50°N are more reliable, the MTZ structure beneath Areas A, B and C corrected by regional tomographic model (Chen et al., 2017) are considered in the following.

3.1. Area A

Beneath Area A which is an N-S elongated zone located in the easternmost part of the study area, the $d410$ is about 15 km shallower and the $d660$ is about 5 km deeper than their normal values, leading to an MTZ that is ∼20 km thicker than normal. An about 25 km thicker-than-normal MTZ is obtained after wavespeed correction (Fig. 7). Seismic tomography and the Benioff Zone geometry (Chen et al., 2017) suggest that the Pacific slab enters the MTZ beneath Area A (Fig. 4). The apparent uplift of the $d410$ beneath Area A is the greatest in the entire study area.

3.2. Area B

Area B is bounded by the 400 and 600 km depth contour lines of the subducting Pacific slab (Fig. 4). In sharp contrast to Area A,

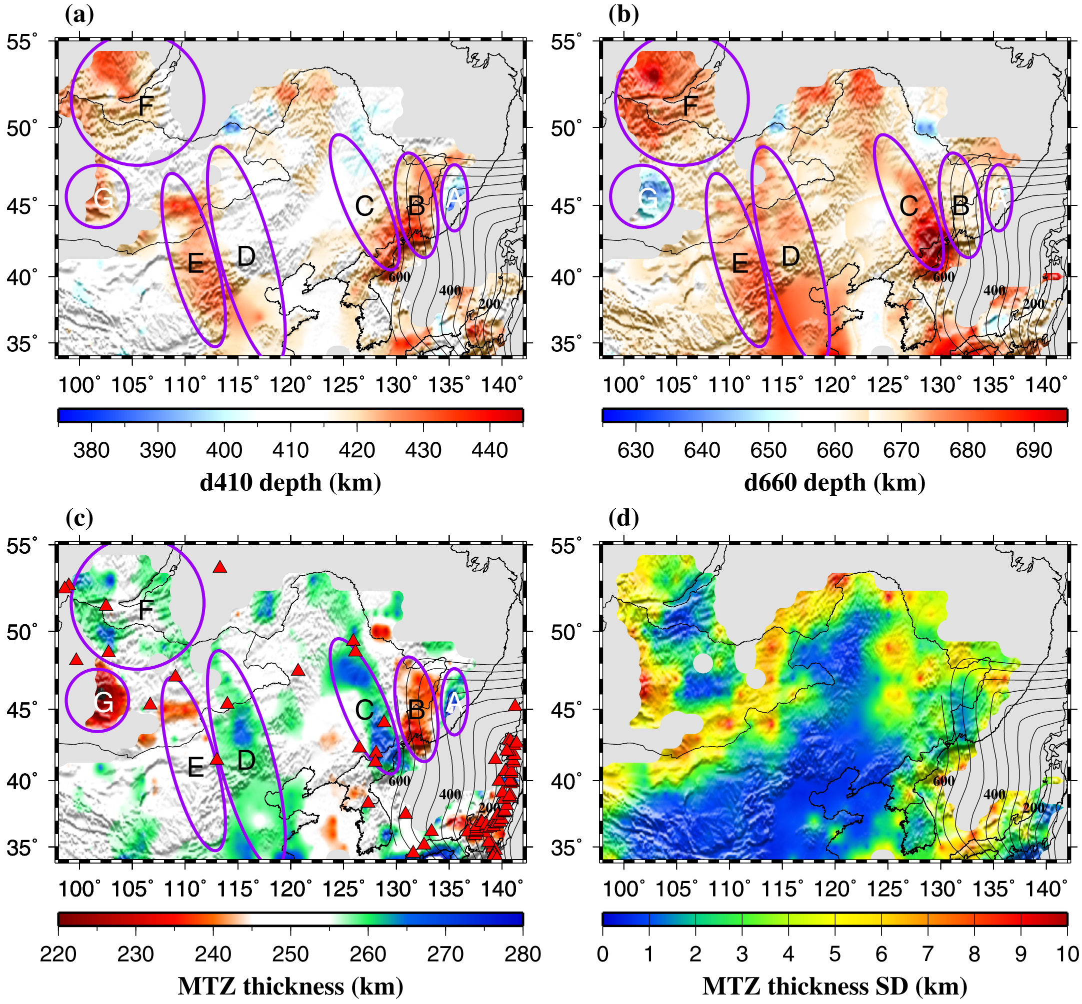

Fig. 4. (a) Spatial distribution of resulting *d*410 apparent depths. (b) Same as (a) but for the *d*660. (c) MTZ thickness measurements. (d) Standard deviation (SD) of the MTZ thickness measurements.

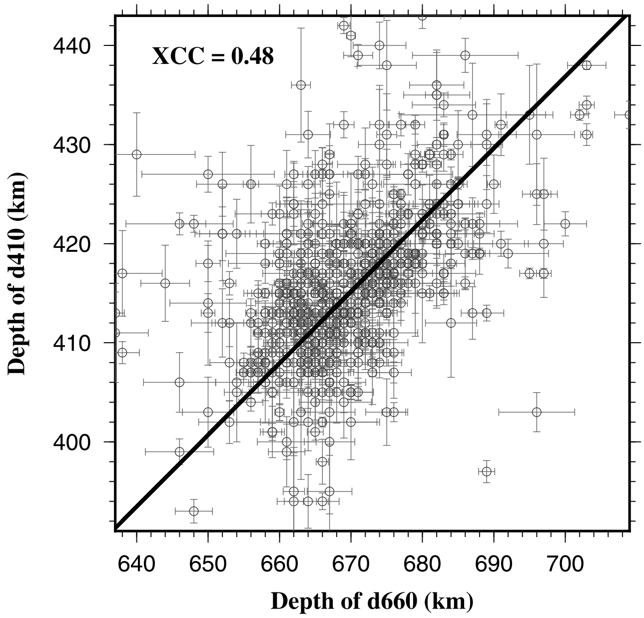

Fig. 5. Correlation plot of apparent *d*410 and *d*660 depths. The line indicates the optimal bivariate regression with a cross-correlation coefficient (XCC) of 0.48.

the apparent depth of the *d*410 beneath this area is about 15 km deeper than normal on average, which is the largest depression of the *d*410 in the study area. The *d*660 in this area is apparently depressed by about 5 km, leading to an approximate 10 km MTZ thinning. The magnitude of MTZ thinning decreases to about 4 km after wavespeed correction (Fig. 7).

3.3. Area C

The NNW-SSE trending Area C follows the Lesser Xing'an Range in the north and the Changbaishan Range in the south, and is mostly surrounded by the Songliao basin. This area is adjacent to the western boundary of the Benioff Zone and is home to most of the Cenozoic volcanoes in NE China (Fig. 4c). This area possesses the largest apparent depression of *d*660 of about 19 km in the entire study area, and the *d*410 depresses by about 7 km, resulting in an MTZ that is about 12 km thicker than normal. This MTZ thickening increases to about 15 km after wavespeed correction (Fig. 7). The NNW-SSE elongated region with thickened MTZ and significant depression of the *d*660 beneath or near the Changbaishan region in the southern part of this area is consistent with previous MTZ studies (Liu et al., 2015; Tian et al., 2016; Zhang et al., 2016).

3.4. Area D

The NNW-SSE trending Area D, which is the largest subarea in this study, consists of (from north to south) the Gobi Desert,

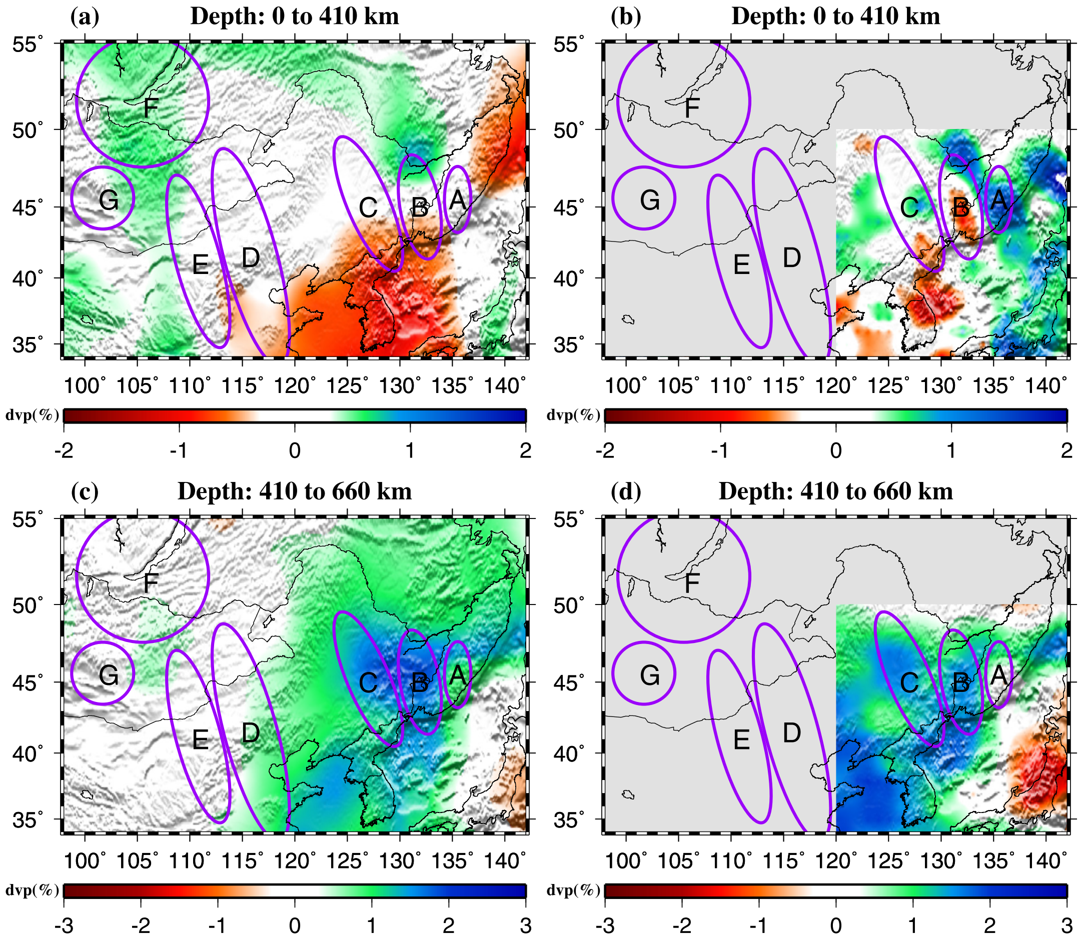

Fig. 6. Averaged P-wavespeed anomalies relative to the IASP91 model above the $d410$ (first row) and MTZ (second row) from previous studies (left panel: Lu et al., 2019; right panel: Chen et al., 2017).

the southern part of the Great Xing'an Range, and the Bohai Bay and North China basins. Similar to Area C, although both the $d410$ (415.6 ± 4.5 km) and $d660$ (674.8 ± 5.1 km) in Area D are apparently deeper than normal, the depression magnitude of the $d660$ is larger than that of the $d410$, resulting in an ~9 km thicker-than-normal MTZ on average. The mean corrected MTZ thickness from the wavespeed model of Lu et al. (2019) is 262.4 ± 5.3 km, which is about 12 km thicker than the global average. Two Cenozoic volcanic fields, the Dariganga in Mongolia and the Datong in north China, are located in the northern part and near the western boundary of this subarea, respectively.

3.5. Area E

Tectonically, this area covers parts of the Mongolian Foldbelt in the north, and the Ordos block and the Shanxi Graben in the south. Beneath this area, both the $d410$ and $d660$ have an apparent depression of about 13 km, resulting in a close to normal MTZ thickness (249.2 ± 6.2 km). Similarly, a close-to-normal MTZ thickness with a mean value of 250.9 ± 7.2 km is observed after wavespeed correction. Chen and Ai (2009) observed significant variations in MTZ thickness between the two sides of the north-south gravity lineament beneath the North China Craton, with an up to 30–40 km MTZ thickening on the eastern side of 114°E and a close-to-normal MTZ on the western side of 114°E. Our observations in Areas D and E are mostly consistent with the patterns reported by Chen and Ai (2009).

3.6. Area F

Area F mainly includes the Baikal rift zone, the southern marginal area of the Siberian platform, and the Altai-Sayan-Baikal foldbelt. This area is dominated by a normal to slightly thickened MTZ with a mean thickness of 256.7 ± 6.4 km, which is mostly caused by a greater apparent depression of the $d660$ (676.3 ± 8.6 km) relative to the $d410$ (418.9 ± 7.5 km). The mean corrected MTZ thickness beneath this area is 254.2±6.4 km, which is slightly thicker than the global average. Although the spatial coverage of Area F and the study areas in previous MTZ studies of the Baikal rift zone (Liu and Gao, 2006; Si et al., 2013) are not exactly the same, a slightly thickened MTZ was also observed by the previous studies.

3.7. Area G

Area G is composed of the Hangay Dome in the north and Altai Mountain in the south. This approximately circular region of about 400 km in diameter is featured by the thinnest MTZ thickness (227.7 ± 8.2 km) in the entire study area resulted from an apparent $d410$ depression of about 10 km and apparent uplift of the $d660$ of 12 km. The corrected MTZ thickness (226.5 ± 8.5 km) is similar to the apparent MTZ thickness. A recent RF study (Chen et al., 2015) has also detected a 10–20 km thinner-than-normal MTZ, but the location with the thinnest MTZ is located about 500 km east of this area.

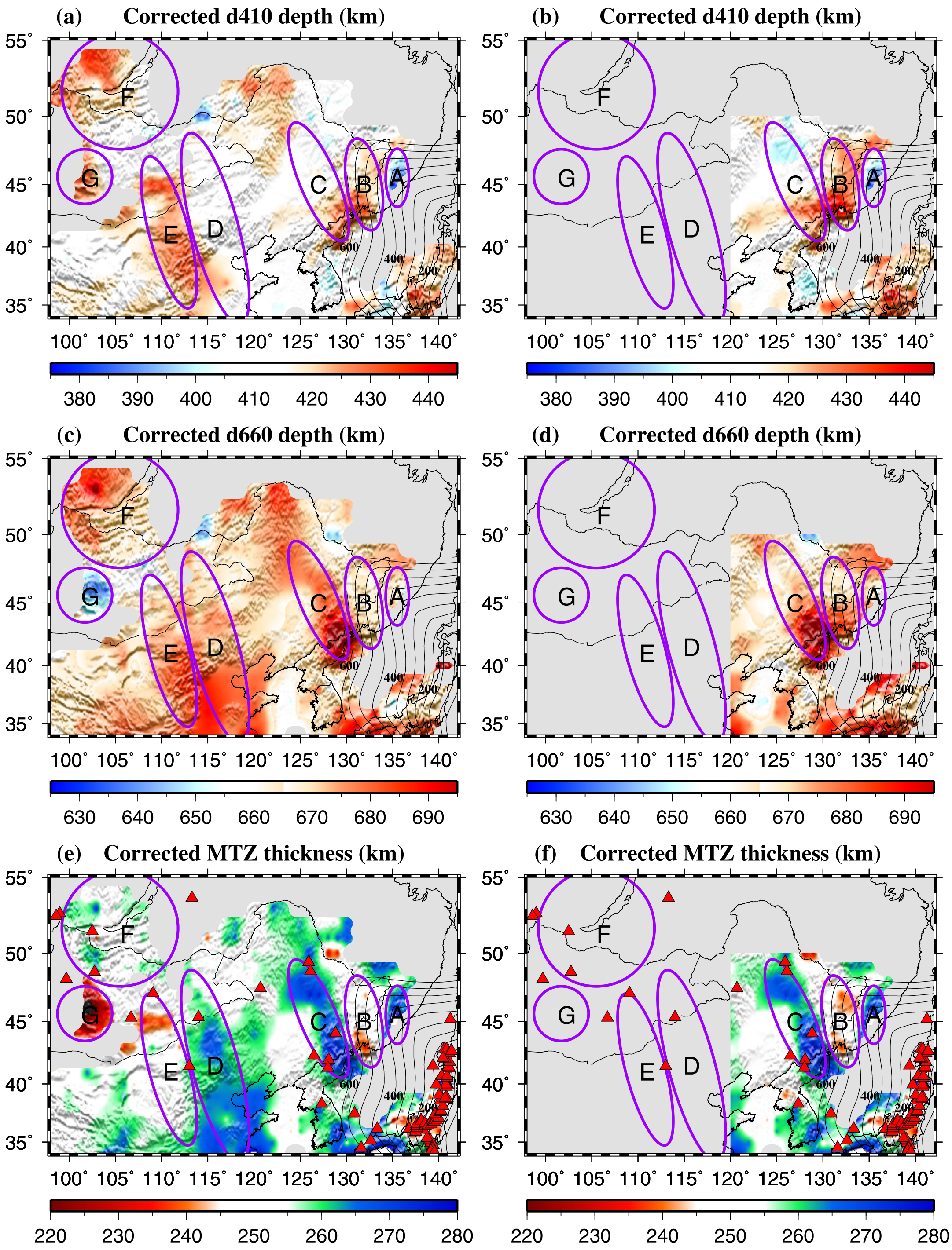

Fig. 7. Corrected depths of $d410$ (first row) and $d660$ (second row), and corrected MTZ thickness (third row) using the wavespeed models of Lu et al. (2019; left panel) and Chen et al. (2017; right panel).

4. Discussion

4.1. *Implications for the depth and lateral extents of the subducted Pacific slab beneath NE Asia*

The resultant systematic spatial variations of the MTZ thickness and apparent discontinuity depths can provide valuable constraints on the geometry and depth extent of the subducted Pacific slab beneath the study area (Fig. 8). Beneath Area A, the ∼20 km apparent thickening of the MTZ can be interpreted by an about −240 K temperature anomaly associated with the subducted slab that enters the MTZ beneath this area. The MTZ thickness beneath Area A after wavespeed correction using the global (Lu et al., 2019) and regional (Chen et al., 2017) models are consistent, which is ∼25 km thicker than normal. Therefore, a higher degree of low temperature anomaly (about −300 K) is required to produce the observation. In Area B, the observed 15 km and 5 km apparent depression of the $d410$ and $d660$, respectively, and the resulting 10 km thinning of the MTZ are attributable to a low wavespeed zone above the $d410$ and a high wavespeed anomaly in the MTZ associated with the subducting slab. If we assume a $d\ln(V_s)/d\ln(V_p)$ value of 1.95, which was found by searching for the optimal $d\ln(V_s)/d\ln(V_p)$ value that minimizes the XCC between the corrected $d410$ and

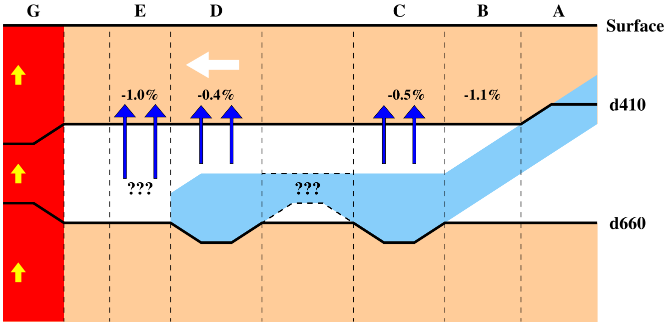

Fig. 8. Schematic sketch of MTZ structure for an E-W profile along 45°N. The blue body is the subducted Pacific slab, and the red column represents thermal upwelling beneath the Hangay Dome. The blue, white, and yellow arrows indicate hydrous migration, plate movement relative to the subducted slab, and thermal upwelling, respectively.

*d*660 depths (Fig. S5) using the approach described in Gao and Liu (2014b), a low wavespeed zone with a mean V_p anomaly of about -1.1% above the *d*410 would result in an apparent depression of 15 km for both the *d*410 and *d*660, while a mean high-wavespeed anomaly of about $+1.2\%$ in the MTZ from the subducting slab would lead to a 10 km apparent uplift of the *d*660. The required wavespeed anomalies above the *d*410 and in the MTZ to produce the observed undulations of the discontinuities are slightly larger than those from previous seismic tomographic studies (Fig. 6). This difference is possibly caused by two reasons. First, the magnitudes of the wavespeed anomalies in this study are estimated under the assumption that the $d\ln(V_s)/d\ln(V_p)$ value is 1.95, which is searched by minimizing the XCC in the whole study area (Fig. S5). The actual $d\ln(V_s)/d\ln(V_p)$ value may be spatially varying due to variable thermal, water-content and other conditions. A larger assumed $d\ln(V_s)/d\ln(V_p)$ value can lead to a reduction of the estimated magnitude of wavespeed anomalies (Fig. S6). Second, the wavespeed anomalies from tomographic studies (Fig. 6) are relative to the mean values rather than absolute values at each depth layer, consequently, the calculated mean wavespeed anomalies using tomographic results may be smaller than the actual values.

A thinned MTZ beneath Area B is also observed by Zhang et al. (2016) but with different shape and magnitude. Zhang et al. (2016) attribute the thinned MTZ to slab tearing associated with stagnation of the descending Pacific plate. However, the MTZ thinning in this area after wavespeed correction is only 3 km for the wavespeed model of Lu et al. (2019), and 4 km for the wavespeed model of Chen et al. (2017). The close-to-normal wavespeed corrected MTZ thickness, when combined with the recent tomographic observations that the slab is continuous and lack of low velocity anomaly in the MTZ, indicates that the apparent MTZ thinning beneath this area is mainly caused by the high velocity anomaly related to the descending Pacific plate in the MTZ, rather than the slab tearing.

The large depression of the *d*660 (19 km) and significant MTZ thickening (12 km) west of the 600 km depth contour line of the top of the subducting Pacific slab imply that the subducted slab contacts closely with the *d*660 in Area C (Figs. 3, 4, and 8). Similarly, an ∼9 km MTZ thickening results from a 6 km apparent depression of the *d*410 and 15 km apparent depression of the *d*660 (Fig. 3) is observed in the Area D. The magnitude of MTZ thickening after wavespeed correction increases to about 12 km, indicating that the thermal or water anomalies exist in the MTZ beneath this area. The existence of a thicker-than-normal MTZ beneath the southern part of Area D is consistent with the observation by a previous MTZ study (Chen and Ai, 2009), which mapped an up to 30–40 km MTZ thickening on the eastern side of 114°E beneath the North China Craton, but is inconsistent with the observation of no obvious variations of MTZ thickness in this area reported by another study (Zhang et al., 2016). Previous tomographic studies (Fig. 6) also show that the leading edge of the stagnant Pacific slab in the MTZ reaches the Great Xing'an Range. Therefore, we speculate that the thickened MTZ beneath Area D is related to the stagnant Pacific slab in the MTZ. Beneath Area E, an ∼12 km depression for both the *d*410 and *d*660 is observed. Both the apparent and wavespeed corrected MTZ thicknesses in Area E are normal (Figs. 4 and 7), which is consistent with the results reported by previous MTZ studies (Chen and Ai, 2009; Zhang et al., 2016), indicating that a cold slab is absent beneath this area. Similarly, this study and the study of Zhang et al. (2016) found that most part of the region between Areas C and D has normal *d*410 and *d*660 depths, suggesting either the absence of a slab, or a thin/thermally normal slab that does not significantly impact the topography of the MTZ discontinuities (Fig. 8).

4.2. Formation mechanism of intraplate volcanoes in NE China

The intraplate Cenozoic volcanoes in NE China, including the Changbaishan, Jingpohu, Longgang, and Wudalianchi, are mainly distributed in Area C which is characterized by an MTZ that is on average 12 km thicker than normal (Fig. 4). The MTZ thickening is due to an 7 km apparent depression of the *d*410 and a 19 km apparent depression of the *d*660 (Fig. 4). The wavespeed corrected MTZ thickness beneath Area C is about 15 km thicker than normal (Fig. 7), which can be attributed to a considerable degree of accumulation of the stagnant slab in the lower MTZ (Chen et al., 2017; Fig. 3). In the following, we use two models involving wavespeed, thermal, and water content anomalies in the upper mantle and MTZ to quantitatively discuss the apparent and wavespeed corrected MTZ discontinuities in this area attempting to associate the volcanism with MTZ structure.

In the model for the apparent depths, if we assume a $d\ln(V_s)/d\ln(V_p)$ value of 1.95 and a slab thickness of 150 km Chen et al., 2017; Tang et al., 2014), a mean V_p anomaly of -0.5% above the *d*410 would lead to an ∼7 km apparent depression of both the *d*410 and *d*660, while a $+2.0\%$ V_p anomaly of the slab in the MTZ can lead to an ∼10 km apparent uplift of the *d*660 (Gao and Liu, 2014a). Additionally, if the scaling relationship of $dV_p/dT = -4.8 \times 10^{-4}$ $\mathrm{km\,s^{-1}\,{}^\circ C^{-1}}$ (Deal et al., 1999) is used, the +2.0% V_p anomaly associated with the stagnant slab would correspond to a -420 K thermal anomaly, which results in an additional depression of the *d*660 by about 15 km if a Clapeyron slope of -1.3 MPa/K (Fei et al., 2004) is used. The net 12 km depression of the *d*660 based on this model is 7 km smaller than the 19 km depression observed in this study.

In the second model, the average V_p anomaly at the depth of 660 km beneath Area C is about $+0.8\%$ (Chen et al., 2017). Under the assumption that the $dV_p/dT = -4.8 \times 10^{-4}$ $\mathrm{km\,s^{-1}\,{}^\circ C^{-1}}$ (Deal et al., 1999), the $+0.8\%$ V_p anomaly corresponds to a -170 K thermal anomaly, leading to an ∼6 km MTZ thickening due to the depression of the *d*660, which is about 9 km smaller than the observed 15 km MTZ thickening. Therefore, both the apparent and wavespeed corrected MTZ structures cannot be explained solely by the negative temperature and corresponding positive wavespeed anomalies related to the stagnant slab in the lower MTZ.

Mineral physics experiments predict that cold and old ($\geq$ 50 Myr) slabs have the capability of carrying water into the MTZ, by hydrous minerals and dense hydrous magnesium silicates (Pearson et al., 2014; Thompson, 1992). Water solubility of wadsleyite and ringwoodite in the slabs reduces with increased temperature (Ohtani et al., 2004), and thus facilitates gradual and long-lasting slab dehydration. Many studies reveal that a high water content exists in the MTZ beneath some areas above the stagnant slabs in NE China (Kelbert et al., 2009), which is considered to be the result of deep dehydration from the stagnant slab. Litasov et al. (2005) indicate that at 1473 K temperature condition, 2 wt.% of water in hydrous peridotite can lead to 15 km depression of the *d*660. If this is the case, the remaining 7–9 km depression of the *d*660 observed in Area C can be attributed to an about 0.9–1.2 wt.% of water content in the lower MTZ, which is slightly higher than the 0.8 wt.% value estimated by Wei et al. (2015) based on seismic tomography. The existence of high water concentration in the MTZ and the long-term (~150 million years) subduction history of the Pacific plate are consistent with the hypothesis that the volcanoes in this area may be related to wet upwelling originated from dehydration of the subducted Pacific slab, a mechanism that has been proposed to explain the loss of cratonic root beneath North China (Zhu et al., 2012) and the formation of Cenozoic volcanoes and continental floods basalts in NE China (Chen et al., 2017; Tian et al., 2016; Wei et al., 2019).

4.3. Possible westward shift of upper mantle low wavespeed anomalies beneath the Datong volcanic field and adjacent area relative to the MTZ

Beneath Area E, an ~13 km apparent depression for both the *d*410 (422.9 ± 7.4 km) and *d*660 (672.6 ± 6.0 km) are observed (Fig. 4). The nearly normal apparent (249.2 ± 6.2 km) and wavespeed corrected MTZ thicknesses (250.9 ± 7.2 km) suggest the absence of velocity and other anomalies in the MTZ beneath this area. A close-to-normal MTZ thickness beneath Area E is also reported by previous MTZ studies (Chen and Ai, 2009; Zhang et al., 2016). The simplest explanation for the observations is a low wavespeed above the *d*410 with a mean V_p anomaly of −1.0%. The magnitude and spatial distribution of the low wavespeed anomalies are in general agreement with seismic tomography results (e.g., Lei, 2012; Li et al., 2018). The Datong volcanic field, the largest Quaternary intraplate volcanic filed in the North China Craton, is located at the boundary between Area E and the adjacent Area D, which is characterized by an ~9 km MTZ thickening. In spite of numerous studies (Huang and Zhao, 2006; Lei, 2012; Li et al., 2018), the causes of the intraplate volcanism remain enigmatic. Proposed models include upwelling of asthenospheric flow along the edge of the thick lithosphere of the Ordos block, and thermal upwelling from the lower mantle (Lei, 2012). The similarity in the NNW-SSE elongated shape and size between Areas E and D may suggest a causative link between the low wavespeeds above the *d*410 beneath Area E and the thickened MTZ beneath Area D. We speculate that similar to Area C, volcanism and low wavespeeds above the *d*410 beneath Area E were initially caused by dehydration of the stagnant Pacific slab currently beneath Area D (Fig. 8). Under this model, the between the low wavespeed upper mantle in Area E and the thickened MTZ in Area D probably suggest a westward movement of the upper mantle beneath Area E relative to the stagnant Pacific slab in the MTZ beneath Area D. However, although the existence of the low wavespeed anomaly above the *d*410 beneath Area E is reported by previous tomographic studies (e.g. Chen et al., 2017), further interdisciplinary investigations are required to test the hypothesis.

4.4. Absence of significant thermal upwelling traversing the MTZ beneath the Baikal Rift

The BRZ (Region F) is characterized by an apparently depressed *d*410 and *d*660 that are 9 and 16 km deeper than normal, respectively, and a slightly thickened MTZ with a magnitude of 7 km (Fig. 4). The apparently depressed MTZ discontinuities indicate that a low wavespeed anomaly exists above the *d*410, which is consistent with previous tomographic studies (e.g., Gao et al., 2003). The MTZ thickness corrected by the global wavespeed model (Lu et al., 2019) is also slightly thicker than normal with a magnitude of 4 km (Fig. 7). Similar to more localized studies (Liu and Gao, 2006; Si et al., 2013), the observed slightly thickened MTZ suggests the present-day absence of a thermal upwelling traversing the MTZ directly beneath the BRZ.

4.5. Thermal upwelling beneath the Hangay Dome and Altai Mountain

The most prominent feature in central Mongolia is an on average 22.3 ± 8.2 km thinning of the MTZ beneath the Hangay Dome and Altai Mountain (Area G) in an approximately circular region of about 400 km in diameter. This thinning is centered at the Hangay Dome and is associated with a 10 km apparent depression of the *d*410 and a 12 km uplift of the *d*660 (Figs. 4 and 7). After wavespeed correction using the global wavespeed model of Lu et al. (2019), an obvious MTZ thinning is still observed with a magnitude of 23 km (Fig. 7). A recent RF study (Chen et al., 2015) reports a 10–20 km thinner-than-normal MTZ beneath the Hangay Dome, and interprets it as the consequence of a slightly warmer thermal anomaly across the MTZ. However, although both studies find a similar magnitude of MTZ thinning beneath the Hangay Dome, there is a significant discrepancy in the distribution of the observed thinned MTZ. In this study, the thinning of the MTZ primarily occurs between 100°E and 105°E, while that revealed in Chen et al. (2015) mainly exists between 104°E and 110°E. This discrepancy is most likely caused by the fact that different stations were used in Chen et al. (2015) and in this study.

One of the simplest interpretations for the thinner-than-normal MTZ in this area is that thermal anomalies beneath the Hangay Dome traverse the whole MTZ from the lower mantle. Assuming Clapeyron slopes of +2.9 MPa/K and −1.3 MPa/K for the *d*410 and *d*660 (Bina and Helffrich, 1994; Fei et al., 2004), respectively, the observed 22–23 km thinning of the MTZ corresponds to a 180–190 K temperature increase in the MTZ. The presence of the thermal anomaly from the lower mantle beneath the Hangay Dome is also evidenced by various studies using different techniques. The integrated seismic study (Chen et al., 2015) finds a thinner-than-normal MTZ and low wavespeed anomalies through the entire MTZ beneath the Hangay Dome. A tomographic study (Zhang et al., 2017) focused on central Mongolia also reveals a low wavespeed zone rooted at least 800 km depth beneath the Hangay Dome, suggesting that a deep thermal upwelling may have caused the uplift of the Hangay Dome and the magmatism of the active Khanuy Gol and Middle Gobi volcanoes. Similarly, using regional gravity data, Zorin et al. (2003) construct 3-dimensional gravity models and reveal the existence of deep thermal upwelling beneath Mongolia, including the Hangay Dome and the Hentay Mountains.

5. Conclusions

Using an unprecedentedly large number of RFs and a non-plane wave RF stacking technique, we imaged the topography of the *d*410 and *d*660 beneath NE Asia. Beneath the study area, a low XCC between the apparent depths of the *d*410 and *d*660 is obtained, suggesting the presence of thermal, water content and wavespeed anomalies in the MTZ. The negative temperature anomaly associated with the subducted Pacific slab is responsible for the three approximately N-S oriented zones with thickened MTZ. Most of the major Cenozoic volcanoes in NE China are underlain by a depressed *d*660 and thickened MTZ, which can be explained by hot and wet upwelling originated from dehydration of the subducted Pacific slab. The strong low wavespeed anomalies above the *d*410 west of the Datong volcanic fields can be explained by the dehydration from the leading portion of the stagnant Pacific slab in the MTZ into the upper mantle, which has shifted toward the west by ~400 km relative to the stagnant slab. The thickened MTZ beneath the BRZ is inconsistent with the present-day existence of active thermal upwelling from the lower mantle. In contrast, the presence of a thermal upwelling from the lower mantle cross the MTZ is indicated by the observed abnormally thinned MTZ beneath the Hangay Dome.

Declaration of competing interest

The authors declare that they have no known competing financial interests or personal relationships that could have appeared to influence the work reported in this paper.

Acknowledgements

Data used in this study were obtained from the IRIS DMC and the Data Management Centre of China National Seismic Network at the Institute of Geophysics, China Earthquake Administration (SEISDMC, http://dx.doi.org/10.7914/SN/CB). We thank three anonymous reviewers and the editor for suggestions that significantly improved the manuscript. The study was supported by the China Postdoctoral Science Foundation to M.S. under grant 2019M661607, the United States National Science Foundation under grant 1919789 to S.G., and the American Chemical Society under grant PRF-60281-ND8 to S.G.

Appendix A. Supplementary material

Supplementary material related to this article can be found online at https://doi.org/10.1016/j.epsl.2019.116040.

References

Ai, Y., Zheng, T., Xu, W., He, Y., Dong, D., 2003. A complex 660 km discontinuity beneath NE China. Earth Planet. Sci. Lett. 212 (1–2), 63–71. https://doi.org/10.1016/S0012-821X(03)00266-8.

Ammon, C.J., 1991. The isolation of receiver effects from teleseismic P waveforms. Bull. Seismol. Soc. Am. 81, 2504–2510.

Bina, C.R., Helffrich, G., 1994. Phase transition Clapeyron slopes and transition zone seismic discontinuity topography. J. Geophys. Res., Solid Earth 99, 15853–15860. https://doi.org/10.1029/94JB00462.

Chen, C., Zhao, D., Tian, Y., Wu, S., Hasegawa, A., Lei, J., Park, J., Kang, I.B., 2017. Mantle transition zone, stagnant slab and intraplate volcanism in NE Asia. Geophys. J. Int. 209 (1), 68–85. https://doi.org/10.1093/gji/ggw491.

Chen, L., Ai, Y., 2009. Discontinuity structure of the mantle transition zone beneath the North China Craton from receiver function migration. J. Geophys. Res., Solid Earth 114 (B6), B06307. https://doi.org/10.1029/2008JB006221.

Chen, M., Niu, F., Liu, Q., Tromp, J., 2015. Mantle-driven uplift of Hangai Dome: new seismic constraints from adjoint tomography. Geophys. Res. Lett. 42 (17), 6967–6974. https://doi.org/10.1002/2015GL065018.

Deal, M.M., Nolet, G., van der Hilst, R.D., 1999. Slab temperature and thickness from seismic tomography: 1. Method and application to Tonga. J. Geophys. Res., Solid Earth 104 (B12), 28789–28802. https://doi.org/10.1029/1999JB900255.

Dueker, K.G., Sheehan, A.F., 1997. Mantle discontinuity structure from midpoint stacks of converted P to S waves across the Yellowstone hotspot track. J. Geophys. Res., Solid Earth 102 (B4), 8313–8327. https://doi.org/10.1029/96JB03857.

Efron, B., Tibshirani, R., 1986. Bootstrap methods for standard errors, confidence intervals, and other measures of statistical accuracy. Stat. Sci. 1 (1), 54–75. https://doi.org/10.1016/j.epsl.2018.09.012.

Fei, Y., Van Orman, J., Li, J., Van Westrenen, W., Sanloup, C., Minarik, W., Hirose, K., Komabayashi, T., Walter, M., Funakoshi, K.-i., 2004. Experimentally determined postspinel transformation boundary in Mg_2SiO_4 using MgO as an internal pressure standard and its geophysical implications. J. Geophys. Res., Solid Earth 109 (B2), B02305. https://doi.org/10.1029/2003JB002562.

Foulger, G.R., Panza, G.F., Artemieva, I.M., Bastow, I.D., Cammarano, F., Evans, J.R., Hamilton, W.B., Julian, B.R., Lustrino, M., Thybo, H., Yanovskaya, T.B., 2013. Caveats on tomographic images. Terra Nova 25 (4), 259–281. https://doi.org/10.1111/ter.12041.

Gao, S.S., Liu, K.H., 2014a. Imaging mantle discontinuities using multiply-reflected P-to-S conversions. Earth Planet. Sci. Lett. 402, 99–106. https://doi.org/10.1016/j.epsl.2013.08.025.

Gao, S.S., Liu, K.H., 2014b. Mantle transition zone discontinuities beneath the contiguous United States. J. Geophys. Res., Solid Earth 119 (8), 6452–6468. https://doi.org/10.1002/2014JB011253.

Gao, S.S., Liu, K.H., Davis, P.M., Slack, P.D., Zorin, Y.A., Mordvinova, V.V., Kozhevnikov, V.M., 2003. Evidence for small-scale mantle convection in the upper mantle beneath the Baikal rift zone. J. Geophys. Res., Solid Earth 108 (B4), 2194. https://doi.org/10.1029/2002JB002039.

Gao, S.S., Liu, K.H., Chen, C., 2004. Significant crustal thinning beneath the Baikal rift zone: new constraints from receiver function analysis. Geophys. Res. Lett. 31 (20), L20610. https://doi.org/10.1029/2004GL020813.

Garth, T., Rietbrock, A., 2017. Constraining the hydration of the subducting Nazca plate beneath Northern Chile using subduction zone guided waves. Earth Planet. Sci. Lett. 474, 237–247. https://doi.org/10.1016/j.epsl.2017.06.041.

Ghosh, S., Ohtani, E., Litasov, K.D., Suzuki, A., Dobson, D., Funakoshi, K., 2013. Effect of water in depleted mantle on post-spinel transition and implication for 660 km seismic discontinuity. Earth Planet. Sci. Lett. 371, 103–111. https://doi.org/10.1016/j.epsl.2013.04.011.

Gripp, A.E., Gordon, R.G., 2002. Young tracks of hotspots and current plate velocities. Geophys. J. Int. 150 (2), 321–361. https://doi.org/10.1046/j.1365-246X.2002.01627.x.

Gudmundsson, O., Sambridge, M., 1998. A regionalized upper mantle (RUM) seismic model. J. Geophys. Res., Solid Earth 103 (B4), 7121–7136. https://doi.org/10.1029/97JB02488.

Huang, J., Zhao, D., 2006. High-resolution mantle tomography of China and surrounding regions. J. Geophys. Res., Solid Earth 111 (B9), 305. https://doi.org/10.1029/2005JB004066.

Kelbert, A., Schultz, A., Egbert, G., 2009. Global electromagnetic induction constraints on transition-zone water content variations. Nature 460 (7258), 1003. https://doi.org/10.1038/nature08257.

Kennett, B.L.N., Engdahl, E.R., 1991. Traveltimes for global earthquake location and phase identification. Geophys. J. Int. 105 (2), 429–465. https://doi.org/10.1111/j.1365-246X.1991.tb06724.x.

Kuritani, T., Kimura, J.I., Ohtani, E., Miyamoto, H., Furuyama, K., 2013. Transition zone origin of potassic basalts from Wudalianchi volcano, NE China. Lithos 156, 1–12. https://doi.org/10.1016/j.lithos.2012.10.010.

Lei, J., 2012. Upper-mantle tomography and dynamics beneath the North China Craton. J. Geophys. Res., Solid Earth 117 (B6), B6313. https://doi.org/10.1029/2012JB009212.

Li, S., Guo, Z., Chen, Y.J., Yang, Y., Huang, Q., 2018. Lithospheric structure of the Northern Ordos from ambient noise and teleseismic surface wave tomography. J. Geophys. Res., Solid Earth 123 (8), 6940–6957. https://doi.org/10.1029/2017JB015256.

Li, X., Yuan, X., 2003. Receiver functions in NE China-implications for slab penetration into the lower mantle in northwest Pacific subduction zone. Earth Planet. Sci. Lett. 216 (4), 679–691. https://doi.org/10.1016/S0012-821X(03)00555-7.

Litasov, K.D., Ohtani, E., Sano, A., Suzuki, A., Funakoshi, K., 2005. Wet subduction versus cold subduction. Geophys. Res. Lett. 32, L13312. https://doi.org/10.1029/2005GL022921.

Liu, K.H., Gao, S.S., 2006. Mantle transition zone discontinuities beneath the Baikal rift and adjacent areas. J. Geophys. Res., Solid Earth 111 (B11), B11301. https://doi.org/10.1029/2005JB004099.

Liu, Z., Niu, F., Chen, Y.J., Grand, S., Kawakatsu, H., Ning, J., Tanaka, S., Obayashi, M., Ni, J., 2015. Receiver function images of the mantle transition zone beneath NE China: new constraints on intraplate volcanism, deep subduction and their potential link. Earth Planet. Sci. Lett. 412, 101–111. https://doi.org/10.1016/j.epsl.2014.12.019.

Lu, C., Grand, S.P., Lai, H., Garnero, E.J., 2019. TX2019 slab: a new P and S tomography model incorporating subducting slabs. J. Geophys. Res., Solid Earth. https://doi.org/10.1029/2019JB017448.

Lysak, S.V., 1984. Terrestrial heat flow in the south of East Siberia. Tectonophysics 103 (1–4), 205–215. https://doi.org/10.1016/0040-1951(84)90084-2.

Mordvinova, V.V., Treussov, A.V., Turutanov, E.K., 2015. Nature of the mantle plume under Hangai (Mongolia) based on seismic and gravimetric data. Dokl. Earth Sci. 460 (3), 334–338. https://doi.org/10.1134/S1028334X15010201.

Ohtani, E., Litasov, K., Hosoya, T., Kubo, T., Kondo, T., 2004. Water transport into the deep mantle and formation of a hydrous transition zone. Phys. Earth Planet. Inter. 143, 255–269. https://doi.org/10.1016/j.pepi.2003.09.015.

Pearson, D.G., Brenker, F.E., Nestola, F., McNeill, J., Nasdala, L., Hutchison, M.T., Matveev, S., Mather, K., Silversmit, G., Schmitz, S., Vekemans, B., Vincze, L., 2014. Hydrous mantle transition zone indicated by ringwoodite included within diamond. Nature 507 (7491), 221–224. https://doi.org/10.1038/nature13080.

Ringwood, A.E., 1975. Composition and Petrology of the Earth's Mantle, 1st ed. McGraw-Hill, New York.

Si, S., Tian, X., Zhang, H., Teng, J., 2013. Prevalent thickening and local thinning of the mantle transition zone beneath the Baikal rift zone and its dynamic implications. Sci. China Earth Sci. 56 (1), 31–42. https://doi.org/10.1007/S11430-012-4547-4.

Sun, M., Fu, X., Liu, K.H., Gao, S.S., 2018. Absence of thermal influence from the African Superswell and cratonic keels on the mantle transition zone beneath southern Africa: evidence from receiver function imaging. Earth Planet. Sci. Lett. 503, 108–117. https://doi.org/10.1016/j.epsl.2018.09.012.

Sun, W., Ding, X., Hu, Y.H., Li, X.H., 2007. The golden transformation of the Cretaceous plate subduction in the West Pacific. Earth Planet. Sci. Lett. 262 (3–4), 533–542. https://doi.org/10.1016/j.epsl.2007.08.021.

Tang, Y., Obayashi, M., Niu, F., Grand, S.P., Chen, Y.J., Kawakatsu, H., Tanaka, S., Ning, J., Ni, J.F., 2014. Changbaishan volcanism in NE China linked to subduction-induced mantle upwelling. Nat. Geosci. 7 (6), 470. https://doi.org/10.1038/NGEO2166.

Thompson, A.B., 1992. Water in the Earth's upper mantle. Nature 358 (6384), 295–302. https://doi.org/10.1038/358295a0.

Tian, Y., Zhu, H., Zhao, D., Liu, C., Feng, X., Liu, T., Ma, J., 2016. Mantle transition zone structure beneath the Changbai volcano: Insight into deep slab dehydration and hot upwelling near the 410 km discontinuity. J. Geophys. Res., Solid Earth 121 (8), 5794–5808. https://doi.org/10.1002/2016JB012959.

Turcotte, D., Schubert, G., 1982. Geodynamics Applications of Continuum Physics to Geological Problems. John Wiley, New York, pp. 1–449.

Wei, W., Zhao, D., Xu, J., Wei, F., Liu, G., 2015. *P* and *S* wave tomography and anisotropy in Northwest Pacific and Eas Asia: constraints on stagnant stab and intraplate volcanism. J. Geophys. Res., Solid Earth 120 (3), 1642–1666. https://doi.org/10.1002/2014JB011254.

Wei, W., Hammond, J.O., Zhao, D., Xu, J., Liu, Q., Gu, Y., 2019. Seismic evidence for a mantle transition zone origin of the Wudalianchi and Halaha volcanoes in NE China. Geochem. Geophys. Geosyst. 20 (1), 398–416. https://doi.org/10.1029/2018GC007663.

Yin, A., 2000. Mode of Cenozoic East-West extension in Tibet suggesting a common origin of rifts in Asia during the Indo-Asian collision. J. Geophys. Res., Solid Earth 105 (B9), 21745–21759. https://doi.org/10.1029/2000JB900168.

Zhang, F., Wu, Q., Grand, S.P., Li, Y., Gao, M., Demberel, S., Ulziibat, M., Sukhbaatar, U., 2017. Seismic wave speed variations beneath central Mongolia: evidence for upper mantle plumes. Earth Planet. Sci. Lett. 459, 406–416. https://doi.org/10.1016/j.epsl.2016.11.053.

Zhang, M., Zhou, X.H., Zhang, J.B., 1998. Nature of the lithospheric mantle beneath NE China: evidence from potassic volcanic rocks and mantle xenoliths. In: Mantle Dynamics and Plate Interactions in East Asia, vol. 27, pp. 197–219.

Zhang, R., Gao, Z., Wu, Q., Xie, Z., Zhang, G., 2016. Seismic images of the mantle transition zone beneath Northeast China and the Sino-Korean craton from P-wave receiver functions. Tectonophysics 675, 159–167. https://doi.org/10.1016/j.tecto.2016.03.002.

Zhu, R.X., Xu, Y.G., Zhu, G., Zhang, H., Xia, Q., Zheng, T., 2012. Destruction of the North China Craton. Sci. China Earth Sci. 55 (10), 1565–1587. https://doi.org/10.1007/s11430-012-4516-y.

Zorin, Y.A., Turutanov, E.K., Mordvinova, V.V., Kozhevnikov, V.M., Yanovskaya, T.B., Treussov, A.V., 2003. The Baikal rift zone: the effect of mantle plumes on older structure. Tectonophysics 371 (1–4), 153–173. https://doi.org/10.1016/S0040-1951(03)00214-2.